International Journal of Advanced Structural Engineering (2019) 11:331–350
https://doi.org/10.1007/s40091-019-00234-w

ORIGINAL RESEARCH

Large deformation analysis of plane-stress hyperelastic problems via triangular membrane finite elements

João Paulo Pascon[1]

Received: 9 March 2018 / Accepted: 24 July 2019 / Published online: 2 August 2019

Abstract

A finite-element formulation based on triangular membranes of any order is proposed to analyze problems involving highly deformable hyperelastic materials under plane-stress conditions. The element kinematics is based on positional description and the degrees of freedom are the current plane coordinates of the nodes. Two isotropic and nonlinear hyperelastic models have been selected: the compressible neo-Hookean model and the incompressible Rivlin–Saunders model. The constitutive relations and the consistent tangent operator are condensed to the compact 2D forms imposing plane-stress conditions. The resultant algorithm is implemented in a computer code. Three benchmark problems are numerically solved to assess the formulation proposed: the Cook's membrane, involving bending, shear, and a singularity point; a partially loaded membrane, which presents severe mesh distortion and large compression levels; and a rubber sealing, which is a more realistic problem. Convergence analysis in terms of displacements, applied forces, and stresses is performed for each problem. It is demonstrated that mesh refinement avoids locking problems associated with incompressibility condition, bending-dominated problems, stress concentration, and mesh distortion. The processing times are relatively small even for fifth-order elements.

Keywords Isoparametric triangular finite elements of any order · Hyperelasticity · Large deformation analysis · Plane-stress condition

Introduction

The Finite-Element Method (FEM) has been widely employed to solve general problems in all branches of engineering. An important application of the FEM is the prediction of the mechanical behavior of structures. There are many types of finite elements in the context of structural engineering: bars (trusses, beams, and frames), two-dimensional elements (membrane, plates, and shells), and three-dimensional (solid) elements. A very simple example is the 2D membrane finite element with triangular geometry, which is the topic of the present paper. This element has been extensively used in plane structural analyses, that is, in predicting the mechanical behavior of structures under plane-stress and plane strain conditions. Such structures are very common in civil, mechanical, and aeronautic engineering, for instance.

Finding the most appropriate finite-element formulation for specific applications remains a major challenge. It is always desirable that the formulation be robust, accurate, reliable and, at the same time, simple. The standard FEM in structural mechanics is displacement-based, i.e., the unknown quantities (or degrees of freedom) are nodal displacements and, in some cases, nodal rotations. The equilibrium of forces is then described via a single-field variational principle, equivalent to Principle of Virtual Work. The strains and stresses are computed from the exact compatibility equations and constitutive laws, respectively. Despite the simplicity of the standard formulation, several alternative techniques have been developed to improve the overall performance of the elements. For example, it is often said that standard 2D finite elements have a poor performance in structural problems involving bending, domains with complex geometries, and near-incompressibility regime. According to Angoshtari et al. (2017), these drawbacks can be overcome using mixed methods, in which the stress field is usually an independent variable and, thus, can

✉ João Paulo Pascon
jppascon@usp.br

[1] Materials Engineering Department, Lorena School of Engineering, University of São Paulo, Pólo-Urbo Industrial, Gleba AI-6, s/no, Lorena, SP 12602-810, Brazil

be computed with higher accuracy when compared to the standard formulation. An example of mixed formulation is the Enhanced Assumed Strain (EAS) method developed by Simo and Rifai (1990), in which the strain field is enriched by adding some incompatible modes. However, mixed methods are considerably more complicated than the standard formulation, increasing the number of degrees of freedom. Another shortcoming of mixed EAS methods is the presence of unphysical (hourglass) instabilities in compression problems. In most cases, the use of an hourglass stabilization technique is required, increasing the complexity of the analysis. Moreover, as pointed out by Jabareen and Rubin (2014), mixed triangular elements may provide an unrealistic soft response in bending-dominated problems.

The element order of approximation considerably affects the numerical results obtained in structural analyses using the FEM. It is well known that high-order elements provide more accurate results, but, on the other hand, demand more computational effort in terms of memory capacity and processing time. Linear order elements, in turn, are very easy to be implemented, simple to be integrated over the domain and provide a fast solution, but, in general, exhibit a very stiff behavior (locking phenomenon) even with an extremely refined mesh. A better performance is usually obtained with triangular elements of quadratic order, but some authors argue that the use of these elements together with full integration provides inaccurate results for nearly incompressible materials (Jabareen and Rubin 2014). Besides, to decrease the processing time for higher order elements, reduced and selective integration techniques have been proposed. However, these methods are complex and case-dependent. For the present author, the accuracy of results when using fully integrated high-order elements is always assured and the large computational effort required can be circumvented by adopting high-performance computers and parallel processing techniques. Following this line of reasoning, the present finite element is the isoparametric triangular membrane element of any order based on positional description and fully integrated. In other words, the order of approximation is general (linear, quadratic, cubic, etc.) and the degrees of freedom are current nodal positions (instead of displacements). High-order elements fully integrated and based on positional FEM have been successfully applied to solve general structural problems in the works of Pascon and Coda (2012, 2013, 2015, 2017), for instance. It has been demonstrated, in these works, that the accuracy of results is guaranteed for sufficiently refined meshes.

The development of finite-element formulations capable of modeling highly deformable materials has received considerable attention over the last decades. In the case of finite displacements, the geometrically nonlinear analysis is imperative, as the change of configuration may be large. In other words, the equilibrium of forces must be achieved at the final deformed configuration, which leads to a nonlinear system of equations regarding the degrees of freedom. However, this system can be solved using standard numerical methods, as the Newton–Raphson iterative technique, which is widely adopted in nonlinear analyses (see, for example, the work of Crisfield 2000).

An example of highly deformable engineering material is the elastomer, which may present large levels of elastic (or reversible) strains. Numerous applications of elastomeric materials can be cited, including bridge bearings, engine parts, vehicle door seals, o-rings, tires, wire insulation, industrial belts, polyurethane foams for car seats, etc. In the case of finite elastic strains, the material behavior is described by hyperelastic constitutive models. The response of a hyperelastic material is expressed via a scalar potential energy density called Helmholtz free-energy function, which must satisfy the following conditions: normality, polyconvexity, and coercivity. The first condition means that the energy is zero when there is no strain. The second requirement is necessary to obtain a unique solution for a given strain or stress field. The third condition is used to prevent the material to be annihilated (the energy tends to infinity when the volume tends to zero) or stretched into an infinite range (the energy must also become infinity when the volume tends to infinity or the strain levels becomes infinitely large). One should note that the linear elastic models, as the Hooke and Saint–Venant–Kirchhoff laws, do not satisfy the polyconvexity and coercivity requirements and, thus, cannot be used to reproduce large levels of elastic strain. Further details regarding hyperelasticity and comparison of the hyperelastic models proposed in the scientific literature can be found, for instance, in the works of Holzapfel (2000) and Pascon (2008).

For general hyperelastic materials, the stress tensor is obtained by differentiating the Helmholtz free-energy function with respect to the strain tensor, which leads to a nonlinear 3D constitutive law; that is, the expressions to obtain the stresses in terms of the strains are nonlinear. In the specific case of plane-stress conditions, a relationship among the strains appears and, thus, the 3D model is condensed into a compact 2D form according to the null stresses. For linear elastic models, the expressions to determine the plane-stresses and the normal out-of-plane strain are all explicit. However, the condensation of the 3D model for plane-stress conditions is not straightforward for nonlinear hyperelastic laws, as the resultant expressions employed to compute stresses in terms of strains are implicit. Two isotropic hyperelastic models are adopted in the present paper: the compressible neo-Hookean law (nH), employed in Sze et al. (2004), for instance; and the incompressible Rivlin–Saunders model (RS), initially proposed by Rivlin (1956) and slightly modified in Pascon (2008). Both models have been extensively employed to reproduce the mechanical response

of elastomers, presenting good agreement with experimental data. In the first case (nH), an implicit and nonlinear relationship among strains must be solved to obtain the out-of-plane strain component. With this component, the plane stresses can be obtained via explicit expressions. For the second model (RS), the strategy of the Lagrangian multiplier is adopted, in which explicit nonlinear expressions are employed to obtain the plane stresses. Although this strategy is well known in the scientific literature, little discussion concerning the consistent tangent operator has been made. Some details regarding this operator, widely employed in nonlinear analyses, are provided in the present paper.

The purpose of this work is to develop a finite-element formulation with isoparametric triangular elements for large deformation analysis of nonlinear hyperelastic materials under plane-stress state. The paper is organized as follows. In "Finite element approximation" section, the finite-element kinematics for triangular elements of any order is described. In "Constitutive modeling" section, the constitutive models employed, as well as the expressions involved in the case of plane-stress conditions, are provided. The equilibrium principle and the numerical algorithm adopted, which are valid for other types of plane elements, are given in "Numerical algorithm" section. The validating numerical examples involving highly deformable materials under plane-stress state are described in "Numerical examples" section. Finally, the concluding remarks drawn from the examples are provided in "Conclusions" section.

Finite-element approximation

In this section, the finite-element kinematics is described together with the deformation measures adopted. The finite element employed in the present work is the isoparametric triangular membrane of any order. The kinematic approximation follows the standard FEM procedure and is based on positional description; that is, it is described in terms of nodal positions and shape functions. The Cartesian planes x_1-x_2 and y_1-y_2 are used to describe, respectively, the initial and the final configurations:

$$x_i = x_i^{\mathrm{k}}\phi_{\mathrm{k}}\left(\xi_1,\xi_2\right) \tag{1}$$

$$y_i = y_i^{\mathrm{k}}\phi_{\mathrm{k}}\left(\xi_1,\xi_2\right), \tag{2}$$

where x_i and y_i are, respectively, the i-component of the initial and final position vector fields ($\boldsymbol{x}$ and $\boldsymbol{y}$); x_i^{k} and y_i^{k} denote, in this order, the initial and final coordinates of node k, whose associated shape function is ϕ_{k}; and the set $\left\{\left(\xi_1,\xi_2\right)\in\Re^2/0\le\xi_1,\xi_2,\xi_1+\xi_2\le 1\right\}$ defines the coordinates of the non-dimensional triangular plane, from which the initial and final configurations are mapped. The degrees of freedom are the current nodal positions (y_i^{k}) instead of nodal displacements, following the positional FEM. The transverse displacements of the mid-surface are restricted, but a transverse normal strain constant along the thickness direction is allowed.

Expressions (1) and (2) can be employed for any order of approximation (linear, quadratic, cubic, etc.). To determine the shape functions for any degree of approximation, the algorithm developed in Pascon and Coda (2013) is adopted here. This general strategy is used to calculate—based on the element order—the number and the non-dimensional coordinates of the nodes, the polynomial coefficients of the shape functions, and their values at any point inside the element domain. Such algorithm is extremely convenient if a finite-element formulation of any order is to be implemented in a computer code, as there is no need to set and write all the shape function coefficients for various orders of approximation, which is very cumbersome especially for high orders.

In this work, the change of configuration is measured using the deformation gradient $\mathbf{F}$, instead of the displacement field $\mathbf{u}=\mathbf{y}-\mathbf{x}$. This kinematic measure is extracted from Nonlinear Continuum Mechanics and is widely employed in nonlinear analyses. The gradient $\mathbf{F}$ can be determined from approximations (1) and (2) following the positional FEM procedure:

$$\mathbf{F} = \frac{\partial \mathbf{y}}{\partial \mathbf{x}} = \mathbf{F}^1\left(\mathbf{F}^0\right)^{-1} \tag{3}$$

$$\mathbf{F}^1 = \frac{\partial \mathbf{y}}{\partial \boldsymbol{\xi}} = \mathbf{y}^{\mathrm{k}}\frac{\partial \varphi_{\mathrm{k}}}{\partial \boldsymbol{\xi}} \tag{4}$$

$$\mathbf{F}^0 = \frac{\partial \mathbf{x}}{\partial \boldsymbol{\xi}} = \mathbf{x}^{\mathrm{k}}\frac{\partial \varphi_{\mathrm{k}}}{\partial \boldsymbol{\xi}}, \tag{5}$$

where the fictitious gradients $\mathbf{F}^0$ and $\mathbf{F}^1$ are the mappings from the non-dimensional plane to the initial and final configurations, respectively. The derivatives of the shape functions can be determined for any order of approximation using the general algorithm mentioned in the last paragraph. One should note that the out-of-plane component F_{33}, which measures the thickness change, is not determined from kinematics, but from the constitutive model adopted, since the deformed body is under plane-stress conditions (see "Constitutive modeling" section). Besides, the components F_{13}, F_{23}, F_{31}, and F_{32} are all null and, thus, only the plane gradient components (F_{11}, F_{12}, F_{21}, and F_{22}) are computed from expressions (3–5).

The strain measure adopted in the present study is the right Cauchy–Green stretch tensor:

$$\mathbf{C} = \mathbf{F}^T\mathbf{F}. \tag{6}$$

As pointed by Holzapfel (2000), this second-order tensor is symmetric, positive-definite, and objective. The symmetry

conditions implies that $C_{ij} = C_{ji}$ (for any indices i and j) and, thus, only three plane components must be determined from the gradient (3): C_{11}, C_{12}, and C_{22}. The mathematical condition of positive definiteness means that tensor $\boldsymbol{C}$ has real positive eigenvalues, which implies that the final length of any material fiber will always be positive. The third condition guarantees that the components of tensor $\boldsymbol{C}$ are not changed by rigid-body motions, that is, have the same values even when the coordinate system is translated or rotated. The transverse components can be related to the thickness via the following expression:

$$C_{33} = \left(F_{33}\right)^2 = \left(\frac{t_F}{t_0}\right)^2, \tag{7}$$

where t_0 and t_F denote, in this order, the initial and the final thickness. Similarly to the deformation gradient, one can write the following equalities: $C_{13} = C_{31} = C_{23} = C_{32} = 0$.

The three scalar invariants of tensor $\boldsymbol{C}$ are also used in the present work:

$$i_1 = tr\mathbf{C} \tag{8}$$

$$i_2 = \frac{1}{2}\left[(tr\mathbf{C})^2 + tr\left(\mathbf{C}^2\right)\right] \tag{9}$$

$$i_3 = J^2 = \det \mathbf{C}, \tag{10}$$

where $tr()$ is the trace operator; and $J = \det\mathbf{F} = (\det\mathbf{C})^{1/2} > 0$ is the Jacobian, which is the local ratio between the current and the initial volume ($J = \mathrm{d}v/\mathrm{d}V_0$). These three invariants can always be employed for isotropic material models and are very common in hyperelasticity (see "Constitutive modeling" section).

Constitutive modeling

The material models adopted to set the mechanical behavior are described in this section. Two isotropic and nonlinear hyperelastic constitutive models have been selected for the present work: compressible neo-Hookean model (Sze et al. 2004) and incompressible Rivlin–Saunders model (Pascon 2008; Rivlin 1956). Both models are usually employed to set the elastic response of elastomers as, for example, carbon-black-filled rubber (Yeoh 1990). The material response of general hyperelastic materials is described in terms of the Helmholtz free-energy function, which is a scalar potential energy density that must satisfy normality, polyconvexity, and coercivity conditions (see, for instance, the work of Holzapfel 2000). In this case, the constitutive law is defined by the stress–strain relationship, which can be found by means of the Clausius–Duhem inequality and the Coleman–Noll entropy principle:

$$\mathbf{S} = J\mathbf{F}^{-1}\boldsymbol{\sigma}\mathbf{F}^{-T} = 2\frac{\partial\psi}{\partial\mathbf{C}}, \tag{11}$$

where $\boldsymbol{S}$ is the second Piola–Kirchhoff stress tensor, defined at the initial (reference) configuration; and $\boldsymbol{\sigma}$ is the Cauchy (or true) stress tensor, defined at the deformed position. Both stress tensor are symmetric and, in the present study, have only plane components, that is: $()_{11}$, $()_{12}$ and $()_{22}$. The stress–strain relations for the two models adopted are given below.

Compressible neo-Hookean model (nH)

The Helmholtz free-energy function for the first model (nH) is as follows:

$$\psi_{nH} = \frac{K}{2}[\ln(J)]^2 + \frac{\mu}{2}\left(i_1 - 3 - 2\ln J\right), \tag{12}$$

where K and μ are the bulk and shear moduli, respectively. As pointed out by Pascon (2008), this model is in accordance with experimental data of elastomers for moderate levels of elastic strains. Combining expressions (11) and (12), one can obtain the nonlinear stress–strain relation for the neo-Hookean model:

$$\mathbf{S}_{nH} = K\ln(J)\mathbf{C}^{-1} + \mu\left(\mathbf{I} - \mathbf{C}^{-1}\right), \tag{13}$$

where $\boldsymbol{I}$ is the identity matrix. The above constitutive law is valid for 3D states of stress and strain. According to Sect. 2, the inverse of tensor $\boldsymbol{C}$ in the case of plane-stress state is as follows:

$$\mathbf{C}^{-1} = \begin{bmatrix} \frac{C_{22}}{C_{11}C_{22}-C_{12}^2} & \frac{-C_{12}}{C_{11}C_{22}-C_{12}^2} & 0 \\ \frac{-C_{12}}{C_{11}C_{22}-C_{12}^2} & \frac{C_{11}}{C_{11}C_{22}-C_{12}^2} & 0 \\ 0 & 0 & \frac{1}{C_{33}} \end{bmatrix}. \tag{14}$$

It should be emphasized that the stretch component C_{33} depends on the plane components; that is, C_{33} is a function of the set $\left(C_{11}, C_{12}, C_{22}\right)$.

The plane-stress conditions at the deformed configuration could be defined for the Cauchy stress tensor $\boldsymbol{\sigma}$. However, it is equivalent to impose such conditions for the second Piola–Kirchhoff stress $\boldsymbol{S}$, since the gradient $\boldsymbol{F}$ has the format showed in (14). One can note that, according to expressions (13) and (14), the components S_{13}, S_{23}, S_{31}, and S_{32} are all null. Therefore, to impose plane-stress conditions, the equality $S_{33} = 0$ can be used. Considering the neo-Hookean model (13), an additional expression is obtained by the following:

$$\left(S_{nH}\right)_{33} = K\ln(J)\frac{1}{C_{33}} + \mu\left(1 - \frac{1}{C_{33}}\right) = 0 \Rightarrow K\ln(J) = \mu\left(1 - C_{33}\right). \tag{15}$$

Inserting this last result into expression (13) leads to the following compact form:

$$\mathbf{S}_{nH} = \mu\left(\mathbf{I} - C_{33}\mathbf{C}^{-1}\right). \tag{16}$$

As one can see, the bulk modulus is eliminated in the plane-stress version. Besides, the nonlinear expressions to determine stresses from the strains are explicit. However, there is no explicit equation to determine the transverse component C_{33} in terms of the plane components (C_{11}, C_{12}, and C_{22}). After some mathematical manipulations, one can obtain the following expressions from the last result in (15):

$$K\ln\left[\sqrt{C_{33}\left(C_{11}C_{22}-C_{12}^2\right)}\right] = \mu\left(1-C_{33}\right) \Rightarrow C_{33}\left(C_{11}C_{22}-C_{12}^2\right) = \left\{\exp\left[\frac{\mu}{K}\left(1-C_{33}\right)\right]\right\}^2. \tag{17}$$

The method to determine the component C_{33} from the plane stretches is provided in "Numerical algorithm" section.

Similar expressions for the plane-stress nH model can be found in the work of Kirchner et al. (1997) considering the left Cauchy–Green stretch tensor ($\mathbf{B} = \mathbf{F}\mathbf{F}^T$), the Kirchhoff stress tensor ($\boldsymbol{\tau} = \mathbf{F}\mathbf{S}\mathbf{F}^T$), and logarithmic stretches. However, the resultant model does not describe the same material response of the present constitutive law because of the different measures adopted in each work.

Incompressible Rivlin–Saunders model (RS)

The nH model cannot reproduce the well-known S-shaped curve of rubber in uniaxial testing (Yeoh 1990), providing an erroneous prediction of the mechanical behavior for extremely large-strain levels. For this reason, more sophisticated hyperelastic models have been proposed to correctly describe the material response in the large-strain regime as, for instance, the Rivlin–Saunders model, initially proposed by Rivlin (1956) for incompressible rubber-like materials:

$$\psi_{\mathrm{RS}} = \sum_{i,j} c_{ij}\left(i_1^{\mathrm{iso}}-3\right)^i\left(i_2^{\mathrm{iso}}-3\right)^j, \tag{18}$$

where c_{ij} are the material coefficients; and the superscript $()^{\mathrm{iso}}$ means isochoric deformation; that is, the volume is preserved: $J=1$. To enforce this condition, the method of Lagrangian multiplier is used, as performed in Pascon (2008), for example:

$$\psi_{\mathrm{RS}} = \psi_{\mathrm{vol}} + \psi_{\mathrm{iso}} = p(J-1) + \sum_{i,j} c_{ij}\left(i_1^{\mathrm{iso}}-3\right)^i\left(i_2^{\mathrm{iso}}-3\right)^j, \tag{19}$$

where p is the Lagrangian multiplier, to be found by the boundary conditions.

The general stress–strain relationship for the RS model is obtained from expressions (11) and (19):

$$\mathbf{S}_{\mathrm{RS}} = \mathbf{S}_{\mathrm{vol}} + \mathbf{S}_{\mathrm{iso}} = p\mathbf{s}_{\mathrm{vol}} + \mathbf{S}_{\mathrm{iso}} \tag{20}$$

$$\mathbf{s}_{\mathrm{vol}} = 2\frac{\partial}{\partial\mathbf{C}}(J-1) = J\mathbf{C}^{-1} \tag{21}$$

$$\begin{aligned}\mathbf{S}_{\mathrm{iso}} &= 2\frac{\partial\psi_{\mathrm{iso}}}{\partial\mathbf{C}} = 2\frac{\partial\psi_{\mathrm{iso}}}{\partial i_1^{\mathrm{iso}}}\frac{\partial i_1^{\mathrm{iso}}}{\partial\mathbf{C}} + 2\frac{\partial\psi_{\mathrm{iso}}}{\partial i_2^{\mathrm{iso}}}\frac{\partial i_2^{\mathrm{iso}}}{\partial\mathbf{C}}\\ &= \alpha\frac{\partial i_1^{\mathrm{iso}}}{\partial\mathbf{C}} + \beta\frac{\partial i_2^{\mathrm{iso}}}{\partial\mathbf{C}}\\ &= 2\left[\sum_{i,j} i c_{ij}\left(i_1^{\mathrm{iso}}-3\right)^{i-1}\left(i_2^{\mathrm{iso}}-3\right)^j\right]\frac{\partial i_1^{\mathrm{iso}}}{\partial\mathbf{C}}\\ &\quad + 2\left[\sum_{i,j} j c_{ij}\left(i_1^{\mathrm{iso}}-3\right)^i\left(i_2^{\mathrm{iso}}-3\right)^{j-1}\right]\frac{\partial i_2^{\mathrm{iso}}}{\partial\mathbf{C}}\end{aligned} \tag{22}$$

$$\frac{\partial i_1^{\mathrm{iso}}}{\partial\mathbf{C}} = \frac{\partial}{\partial\mathbf{C}}tr\mathbf{C} = \mathbf{I} \tag{23}$$

$$\frac{\partial i_2^{\mathrm{iso}}}{\partial\mathbf{C}} = \frac{1}{2}\frac{\partial}{\partial\mathbf{C}}\left[(tr\mathbf{C})^2 + tr\left(\mathbf{C}^2\right)\right] = (tr\mathbf{C})\mathbf{I} + \mathbf{C}, \tag{24}$$

where α and β are scalar auxiliary variables. Since the material is considered to be incompressible, the volumetric stress $\mathbf{s}_{\mathrm{vol}}$ is equal to $\mathbf{C}^{-1}$. One can note that the nH model (13) is relatively more simple than the RS model.

The Lagrangian multiplier must be found to completely determine the stress components. Considering plane-stress conditions together with incompressibility:

$$\left(S_{\mathrm{RS}}\right)_{33} = p\left(s_{\mathrm{vol}}\right)_{33} + \left(S_{\mathrm{iso}}\right)_{33} = 0 \Rightarrow p = -\frac{\left(S_{\mathrm{iso}}\right)_{33}}{\left(s_{\mathrm{vol}}\right)_{33}} = -\left(S_{\mathrm{iso}}\right)_{33}C_{33}. \tag{25}$$

Unlike the first model, there is an explicit expression to obtain the strain component C_{33} in terms of the plane components for the present model:

$$J^2 = C_{33}\left(C_{11}C_{22}-C_{12}^2\right) = 1 \Rightarrow C_{33} = \frac{1}{C_{11}C_{22}-C_{12}^2}. \tag{26}$$

Therefore, the plane version for the RS model results in the following:

$$\mathbf{S}_{\mathrm{RS}} = -\left(S_{\mathrm{iso}}\right)_{33}C_{33}\mathbf{s}_{\mathrm{vol}} + \mathbf{S}_{\mathrm{iso}}. \tag{27}$$

One should remember that both expressions (15) and (27) are plane compact forms, i.e., the matrices that appear have dimensions 2×2.

The RS model adopted here can be considered as a general set of hyperelastic models, differing from each other

in terms of the coefficients adopted. Three common specific models can be cited by the following:

$$\psi_{\mathrm{MR}} = c_{10}\left(\bar{I}_1^{\mathrm{iso}} - 3\right) + c_{01}\left(\bar{I}_2^{\mathrm{iso}} - 3\right) \tag{28}$$

$$\psi_{Y} = c_{10}\left(\bar{I}_1^{\mathrm{iso}} - 3\right) + c_{20}\left(\bar{I}_1^{\mathrm{iso}} - 3\right)^2 + c_{30}\left(\bar{I}_1^{\mathrm{iso}} - 3\right)^3 \tag{29}$$

$$\begin{aligned}\psi_{\mathrm{BBC}} = {} & c_{10}\left(\bar{I}_1^{\mathrm{iso}} - 3\right) + c_{20}\left(\bar{I}_1^{\mathrm{iso}} - 3\right)^2 + c_{30}\left(\bar{I}_1^{\mathrm{iso}} - 3\right)^3 \\ & + c_{01}\left(\bar{I}_2^{\mathrm{iso}} - 3\right) + c_{02}\left(\bar{I}_2^{\mathrm{iso}} - 3\right)^2,\end{aligned} \tag{30}$$

where ψ_{MR} represents the Mooney–Rivlin model (Mooney 1940); ψ_Y denotes the Yeoh model (Yeoh 1990); and ψ_{BBC} corresponds to the Bechir–Boufala–Chevalier model (Bechir et al. 2002). The three hyperelastic models (28–30) have been proposed for incompressible rubber-like materials based on experimental data.

Numerical algorithm

In this section, the equilibrium principle and the numerical algorithm adopted in the present study are described. The static equilibrium of the structure is achieved by means of the Principle of Minimum Total Potential Energy, which is equivalent to the nonlinear version of the Principle of Virtual Work:

$$\Pi = \int_{\Omega_0} \psi \mathrm{d}V_0 - \mathbf{f}_{\mathrm{ext}} \cdot \mathbf{y} \tag{31}$$

$$\delta\Pi = \frac{\partial \Pi}{\partial \mathbf{y}} \cdot \mathbf{y} = 0 \Rightarrow \int_{\Omega_0} \frac{\partial \psi}{\partial \mathbf{y}} \mathrm{d}V_0 = \mathbf{f}_{\mathrm{ext}}, \tag{32}$$

where scalar Π is the total potential energy; $\mathrm{d}V_0$ is a volume element of the initial domain Ω_0; $\boldsymbol{f}_{\mathrm{ext}}$ is the vector of applied (external) forces; symbol δ denotes a virtual variation; and $\boldsymbol{y}$, in this case, is the vector that contains all the current nodal positions, i.e., is the vector of degrees of freedom. Although the integration is performed at the initial configuration, the equilibrium is reached at the current position; that is, the analysis is geometrically nonlinear. This equilibrium is described in the result of expression (32), in which the integral corresponds to the vector of internal forces ($\mathbf{f}_{\mathrm{int}}$).

The equilibrium $\mathbf{f}_{\mathrm{int}} = \mathbf{f}_{\mathrm{ext}}$ in expression (32) denotes a nonlinear system of equations regarding the degrees of freedom ($\mathbf{y}$). Consequently, for general prescribed forces, analytical solutions in terms of positions are not available. To solve this problem, the Newton–Raphson iterative technique is employed by the following:

$$\mathbf{r} = \int_{\Omega_0} \frac{\partial \psi}{\partial \mathbf{y}} \mathrm{d}V_0 - \mathbf{f}_{\mathrm{ext}} \tag{33}$$

$$\mathbf{r} + \frac{\partial \mathbf{r}}{\partial \mathbf{y}} \cdot \Delta\mathbf{y} = \mathbf{0} \Rightarrow \Delta\mathbf{y} = -\mathbf{H}^{-1} \cdot \mathbf{r} \tag{34}$$

$$\mathbf{H} = \int_{\Omega_0} \frac{\partial^2 \psi}{\partial \mathbf{y} \partial \mathbf{y}} \mathrm{d}V_0, \tag{35}$$

where $\boldsymbol{r}$ is the residual force vector; and $\boldsymbol{H}$ is the Hessian matrix. One can note that the external forces are conservative, i.e., do not depend on the current positions. The position vector $\boldsymbol{y}$ is iteratively updated via (34) until the residual vector $\boldsymbol{r}$ is sufficiently small. The equilibrium is numerically satisfied when the following norm is smaller than a given tolerance:

$$e = \frac{\sum \left(r_i\right)^2}{\sum \left(x_i\right)^2} \tag{36}$$

where $\boldsymbol{x}$, in this case, is the vector that contains all the initial nodal positions. The summation in (36) is performed regarding only the degrees of freedom that are not restricted. The Newton–Raphson method, although computationally expensive, is often employed in nonlinear analyses because of the quadratic rate of convergence. In this work, the prescribed loads (or displacements) are divided into a large number of steps to improve the convergence and to decrease the chance of numerical instabilities.

The first and the second derivatives of ψ that appear in expressions (32) and (35) are determined as follows:

$$\frac{\partial \psi}{\partial \mathbf{y}} = \frac{\partial \psi}{\partial \mathbf{C}} : \frac{\partial \mathbf{C}}{\partial \mathbf{y}} = \frac{1}{2}\mathbf{S} : \frac{\partial \mathbf{C}}{\partial \mathbf{y}} \tag{37}$$

$$\frac{\partial^2 \psi}{\partial \mathbf{y} \partial \mathbf{y}} = \frac{1}{2}\left(\frac{\partial \mathbf{S}}{\partial \mathbf{C}} : \frac{\partial \mathbf{C}}{\partial \mathbf{y}} : \frac{\partial \mathbf{C}}{\partial \mathbf{y}} + \mathbf{S} : \frac{\partial^2 \mathbf{C}}{\partial \mathbf{y} \partial \mathbf{y}}\right). \tag{38}$$

The derivatives of stretch tensor $\boldsymbol{C}$ with respect to the degrees of freedom $\boldsymbol{y}$ can be found by means of differentiation procedures in tensor algebra. A solid version to determine such derivatives can be found, for instance, in the work of Pascon (2012), in which any order tetrahedral elements are employed. The fourth-order tensor $\wp = \partial \mathbf{S} / \partial \mathbf{C}$ is the consistent tangent operator, which is defined according to the stress–strain relationship. Applying this concept to the neo-Hookean compact form (16) leads to:

$$\wp_{nH} = -\mu\left(\mathbf{C}^{-1} \otimes \frac{\partial C_{33}}{\partial \mathbf{C}} + C_{33}\frac{\partial \mathbf{C}^{-1}}{\partial \mathbf{C}}\right), \tag{39}$$

where the symbol $\otimes$ denotes tensor product. The derivatives of C_{33} and $\boldsymbol{C}^{-1}$ in terms of tensor $\boldsymbol{C}$ are provided in "Appendix 1". As mentioned before (see "Compressible neo-Hookean model (nH)" section), a numerical strategy is

used to determine the transverse strain component C_{33} from the plane strain components. A method similar to the Newton–Raphson procedure is employed (see expression 15):

$$r_{C33} = C_{33}\left(C_{11}C_{22} - C_{12}^2\right) - \left\{\exp\left[\frac{\mu}{K}\left(1 - C_{33}\right)\right]\right\}^2 \quad (40)$$

$$r_{C33} + \frac{\mathrm{d}r_{C33}}{\mathrm{d}C_{33}}\Delta C_{33} = 0 \Rightarrow \Delta C_{33} = -\left(\frac{\mathrm{d}r_{C33}}{\mathrm{d}C_{33}}\right)^{-1} r_{C33} \quad (41)$$

$$\frac{\mathrm{d}r_{C33}}{\mathrm{d}C_{33}} = C_{11}C_{22} - C_{12}^2 + 2\frac{\mu}{K}\left\{\exp\left[\frac{\mu}{K}\left(1 - C_{33}\right)\right]\right\}^2. \quad (42)$$

The component C_{33} is iteratively updated until r_{C33} is sufficiently small.

The consistent tangent operator for the RS model is obtained from (27):

$$\wp_{\mathrm{RS}} = -\mathbf{s}_{\mathrm{vol}} \otimes \left[\frac{\partial\left(S_{\mathrm{iso}}\right)_{33}}{\partial \mathbf{C}} C_{33} + \left(S_{\mathrm{iso}}\right)_{33}\frac{\partial C_{33}}{\partial \mathbf{C}}\right] - \left(S_{\mathrm{iso}}\right)_{33} C_{33}\frac{\partial \mathbf{s}_{\mathrm{vol}}}{\partial \mathbf{C}} + \frac{\partial \mathbf{S}_{\mathrm{iso}}}{\partial \mathbf{C}}. \quad (43)$$

The derivatives in terms of tensor $\boldsymbol{C}$ are given in "Appendix 2". The dimensions of the consistent tangent operators (39) and (43) are $2\times2\times2\times2$.

All the volume integrals that appear in the present section are numerically evaluated by the following:

$$\int_{\Omega_0} g\mathrm{d}V_0 = t_0 \int_{\xi} gJ_0\mathrm{d}\xi_1\mathrm{d}\xi_2 = t_0 \sum_{i=1}^{\mathrm{nip}} \left(gJ_0 w\right)_i, \quad (44)$$

where g is a the general function to be integrated over the reference initial domain; J_0 is the Jacobian of the fictitious transformation defined in (5); that is, $J_0 = \det\left(\mathbf{F}^0\right)$; nip is the number of integration points; and w denotes the weight of each point.

A summary of the algorithm implemented is provided in the flowchart of Fig. 1.

Numerical examples

In this section, the performance of the finite-element formulation developed is assessed. To this end, three structural problems involving highly deformable hyperelastic materials under plane-stress conditions are numerically analyzed: the Cook's membrane, a partially loaded membrane, and a rubber sealing.

The formulation proposed is implemented in a computational code written in FORTRAN language and, thus, the numerical results are obtained from computer simulations. To this end, a parallel processing technique in a cluster with 12 processors has been used. Comparison with numerical results from the scientific literature is performed to validate the present methodology. The tolerance adopted for the errors (36) and (40) in all the examples is 10^{-6}.

Several meshes are employed for all the examples to analyze the influence of the mesh refinement on the accuracy of results. Both hierarchical and polynomial refinements are used, that is, the number and the order of the elements are increased until there is convergence of results. To perform this convergence analysis, all the meshes are generated from

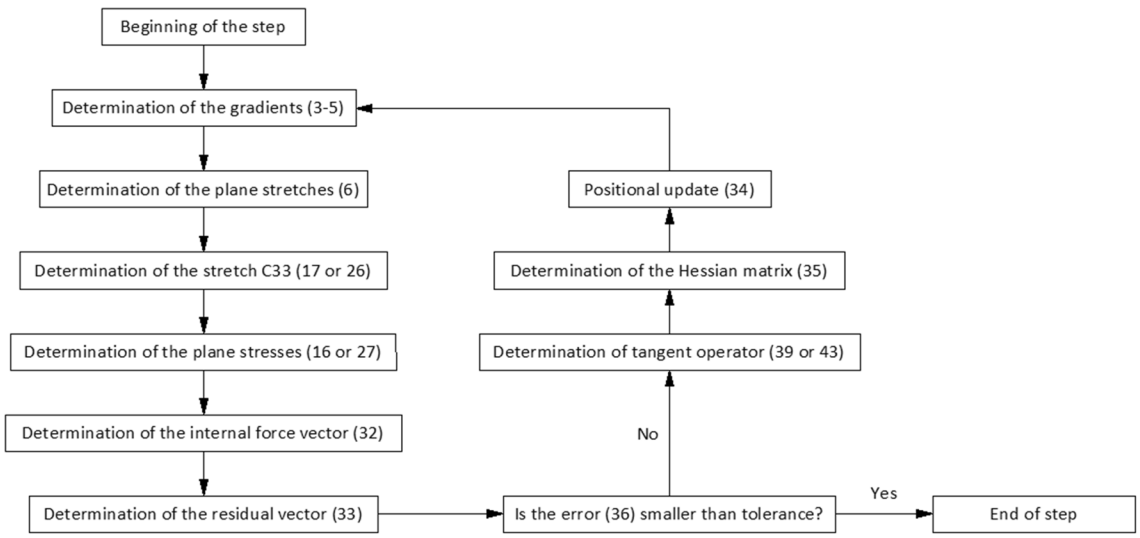

Fig. 1 Flowchart of the algorithm implemented

the same base mesh. The nodes are equally spaced for each quadrilateral of the base mesh.

In most of the finite-element papers, only the displacement fields are analyzed. However, the stress level control is also extremely important for design purposes. The stress values at the nodes are calculated in a post-processing code. After simulating the structure with the main program, the approximated displacement fields at the end of some specific steps are stored. Based on these fields, which are represented by the vector of degrees of freedom, one can determine strains and stresses at any point inside the domain. Since a general node can belong to various elements, the stress values at this node obtained for each element may be different. Therefore, the stresses are determined previously at the numerical integration points and then transferred to the nodes via a linear interpolation based on the least-squares method. For the nodes that belong to more than one element, a simple average of the nodal stresses is used. It should be said that another numerical strategies for stress field determination could be employed and compared to the present one.

Cook's membrane

The first example is the Cook's membrane showed in Fig. 2. According to Mostafa et al. (2013), this popular benchmark problem has been proposed by Cook and Malkus (1989). The objective of simulating this example is to test the performance of finite elements in a problem with combined bending and shear, together with a singularity at the upper left corner. As pointed out by Düster et al. (2003), the difficulties in analyzing this problem are the high distortion of the elements and the strong deformation of the mesh around the singularity point. The uniform vertical load at the right face is divided into 100 steps. All the degrees of freedom of the left boundary are restricted to reproduce the clamped condition. The base mesh depicted in Fig. 2 has been proposed to refine the most critical regions, in which the stress and strain fields are expected to be more complex.

Three material models have been selected to analyze the present example, according to Fig. 2. The vertical load reaches the value of 40 N/mm for the nH model and 0.4 N/mm for the other two models. The coefficients of the nH model are the same as those adopted in Angoshtari et al. (2017) and Sze et al. (2004) for a generic near-incompressible material. The use of a bulk modulus K much larger than the shear modulus μ leads to a material model in which the volumetric strength is high and, thus, the volume changes are small. The material coefficients for the MR and BBC models have been interpolated in the work of Pascon (2008) from the experimental data of Yeoh (1997) for unfilled natural rubber vulcanizates, considering the incompressibility condition.

The convergence analysis in terms of displacements is performed for the right top corner and considering only the nH and BBC models. The plane displacements of this corner converge with mesh refinement for both models, according to Tables 1 and 2. One can note that the vertical displacement (u_2) converges slightly faster than the horizontal displacement (u_1). The convergence is reached quickly and easily, since the processing times and the number of iterations per step are relatively small. As expected, the present rate of convergence regarding displacements is improved by increasing the element order, since the required number of degrees of freedom becomes smaller for the higher orders. A similar convergence rate is obtained in Düster et al. (2003), in which shell-like solid elements with independent approximations along the three spatial directions are employed. In that work, the Cook's membrane is analyzed

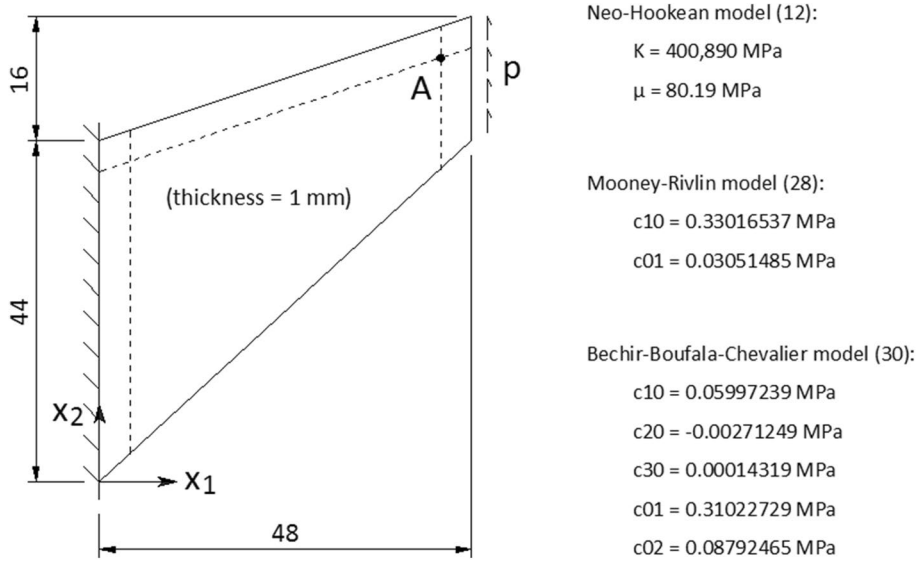

Fig. 2 Cook's membrane: geometry, boundary conditions, and material coefficients (the dashed lines denote the base mesh)

Table 1 Convergence analysis regarding displacements for the nH model

ORD	NDOF	NE	NIP	u_1	u_2	PT (s)	TNI
1	24	12	1	−11.33	19.69	1	300
	70	48		−20.26	24.17	1	300
	234	192		−25.24	25.55	1	301
	850	768		−27.18	25.97	1	300
	1850	1728		−27.62	26.06	2	300
	3234	3072		−27.79	26.11	4	300
	5002	4800		−27.88	26.13	8	300
	7154	6912		−27.93	26.15	11	311
2	70	12	12	−24.87	25.56	1	313
	234	48		−27.55	26.00	1	311
	494	108		−27.88	26.10	1	306
	850	192		−27.96	26.13	2	302
	1302	300		−28.00	26.15	3	300
	1850	432		−28.03	26.17	5	300
3	140	12	13	−27.60	25.91	1	339
	494	48		−27.99	26.14	1	336
	1064	108		−28.05	26.19	2	347
	1850	192		−28.09	26.21	4	353
	2852	300		−28.11	26.22	8	359
	4070	432		−28.27	26.30	14	381
4	234	12	16	−27.95	26.12	1	313
	850	48		−28.08	26.20	4	324
	1850	108		−28.08	26.20	15	300
	3234	192		−28.10	26.21	26	291
5	352	12	19	−28.10	26.22	2	336
	1302	48		−28.09	26.20	18	322
	2852	108		−28.11	26.22	35	320
	5002	192		−28.12	26.22	119	300

ORD, element order; NDOF, number of degrees of freedom; NE, number of elements; NIP, number of integration points (per element); u_1 and u_2, displacements of the right top corner (mm); PT (s), processing time (in seconds); TNI, total number of iterations

using the Hartmann–Neff model, which is another nonlinear hyperelastic relation for near-incompressible rubber-like materials. Besides, the number of elements in that work is constant and equal to six, while the order of approximation is increased from linear to seventh degree. In the case of a linear approximation along the thickness direction, which is equivalent to the present finite-element formulation, the mesh of fifth degree with approximately 400 degrees of freedom is sufficient in terms of displacements. The convergence rate for the cubic and fourth degrees obtained here is comparable, for example, to the mixed finite-element formulations of Chavan et al. (2007) and Mostafa et al. (2013). In the first work, a modified three-field variational principle is employed with a general hyperelastic model. In the second study, a variation of the assumed strain approach, called the Assumed Natural Deviatoric Strain concept, is employed to develop a high-performance quadrilateral element of linear order. According to Tables 1 and 2, the numerical results obtained with the fifth order practically do not change by increasing the amount of elements. This convergence behavior is also obtained for the Cook's membrane in the work of Angoshtari et al. (2017), in which a new class of mixed finite elements, called compatible strain mixed finite-element methods (CSFEM), is introduced. In the last three works cited, it is demonstrated that the alternative formulations proposed have a better performance than the pure-displacement FEM. However, the authors compare the convergence rate of their finite elements with that obtained through linear order standard elements, which obviously present severe locking behavior for coarse meshes. Another important issue to be highlighted is that the mesh employed in the present work and in Düster et al. (2003) present a more refinement level around the singularity point, while the mesh employed in the other three studies is regular (that is, the four edges of the panel are equally divided).

Table 2 Convergence analysis regarding displacements for the BBC model

ORD	NDOF	NE	NIP	u_1	u_2	PT (s)	TNI
1	24	12	1	−10.75	20.45	1	300
	70	48		−19.75	25.37	1	300
	234	192		−25.24	27.35	1	300
	850	768		−27.90	28.20	1	270
	1850	1728		−28.58	28.40	2	252
	3234	3072		−28.85	28.49	4	241
	5002	4800		−28.98	28.53	6	233
	7154	6912		−29.06	28.56	8	230
2	70	12	13	−25.13	27.61	1	300
	234	48		−28.53	28.36	1	300
	494	108		−29.02	28.52	1	300
	850	192		−29.13	28.57	2	275
	1302	300		−29.18	28.59	3	262
	1850	432		−29.20	28.60	4	254
3	140	12	16	−28.58	28.20	1	339
	494	48		−29.17	28.57	1	336
	1064	108		−29.21	28.60	2	347
	1850	192		−29.23	28.62	4	353
	2852	300		−29.24	28.63	8	359
	4070	432		−29.25	28.63	14	381
4	234	12	19	−29.13	28.54	1	300
	850	48		−29.21	28.61	5	279
	1850	108		−29.23	28.62	12	264
	3234	192		−29.24	28.63	13	244
5	352	12	46	−29.18	28.58	4	300
	1302	48		−29.23	28.62	14	265
	2852	108		−29.24	28.63	32	245
	5002	192		−29.24	28.63	46	235

ORD, element order; NDOF, number of degrees of freedom; NE, number of elements; NIP, number of integration points (per element); u_1 and u_2, displacements of the right top corner (mm); PT (s), processing time (in seconds); TNI, total number of iterations

The convergence analysis in terms of stresses is performed considering the point A depicted in Fig. 2. The reason for selecting this point is the proximity to the loaded edge and the distance to the singularity point, at which the stress concentration may lead to unreasonable vales. In addition to the plane stresses, the equivalent Cauchy stress is determined by the following:

$$\sigma_{\text{eq}} = \sqrt{\frac{3}{2}\text{dev}\boldsymbol{\sigma} : \text{dev}\boldsymbol{\sigma}} = \sqrt{\left(\sigma_1^2 + \sigma_2^2 - \sigma_1\sigma_2 + 3\tau_{12}^2\right)}, \tag{45}$$

where $\text{dev}\boldsymbol{\sigma}$ is the deviatoric Cauchy stress tensor. According to Figs. 3 and 4, the stress values converge with mesh refinement. However, the trend of improving the rate of convergence by increasing the order, which is observed for displacements, is not clear for the stresses. In general, the convergence rate of stresses is better for the nH model. The equivalent stress (45) for the BBC model, for instance, has a poor convergence rate for the linear, fourth, and fifth orders. Considering the nH model, the quadratic and cubic orders present a similar convergence rate of that obtained in Mostafa et al. (2013). Moreover, the less refined fifth-order meshes present very different results when compared to the corresponding solutions. This order was expected to provide a good solution even for coarse meshes, as in the study of Angoshtari et al. (2017). These convergence rate problems may be related to the numerical strategy employed to obtain the stress values (determined from a simple average of numerical integration values linearly interpolated). Another possible reason is the approximation adopted for the displacement field along the thickness direction. In the work of Düster et al. (2003), for instance, the linear approximation (or constant strain) across the thickness is sufficient for a good rate of convergence regarding the displacements of the right top corner and the equivalent stress at a point close to point A. However, for individual stress components, the

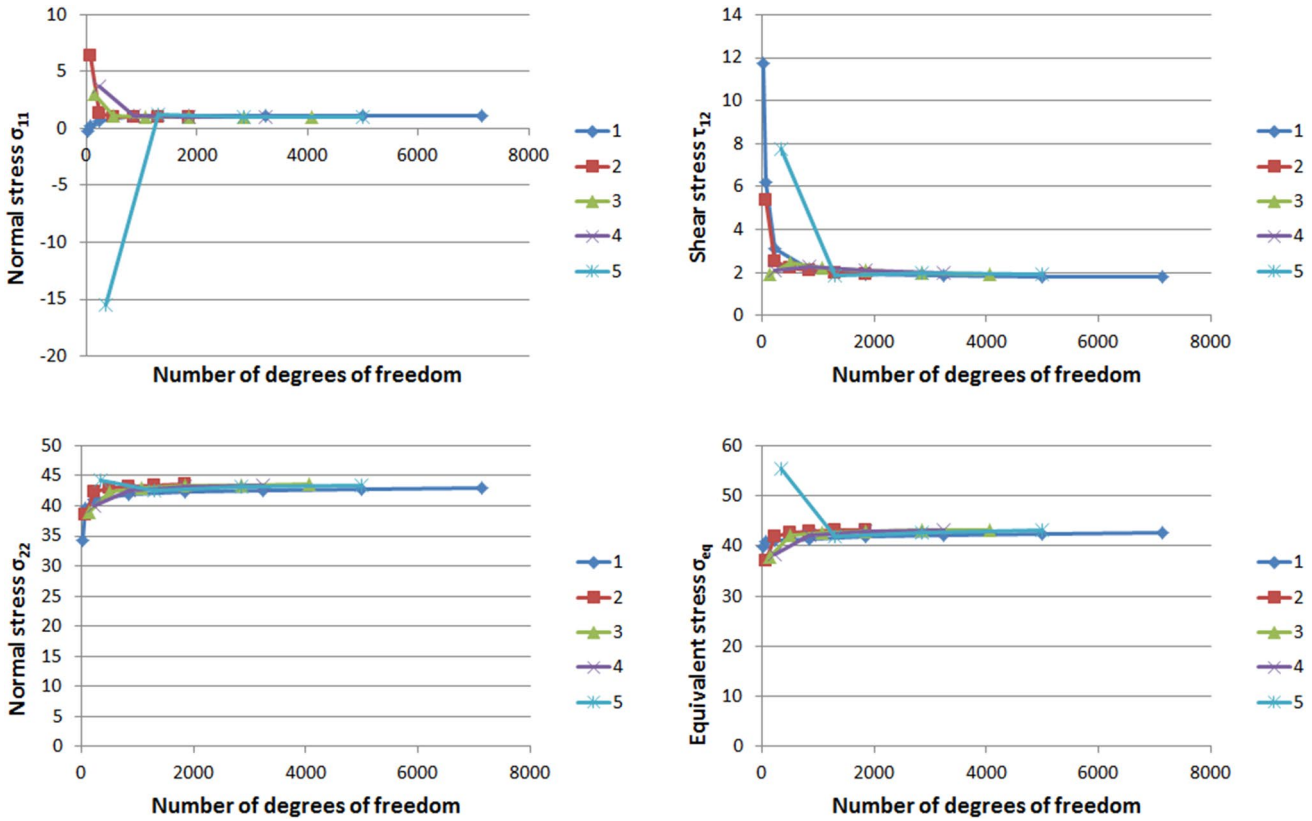

Fig. 3 Convergence analysis in terms of stresses (in kPa) for the nH model at point A (44.0, 58.6667)

quadratic order (or linear strain) along the thickness direction is required. It should be pointed out that, in the work of Düster et al. (2003), the approximation adopted for the three directions are based on the standard (pure-displacement) FEM procedure, i.e., no mixed or enhanced methods are employed. The need of enriching the kinematics across the thickness direction of the Cook's membrane is probably related to the fact that the stress field around the singularity point has a three-dimensional character, which cannot be reproduced with the present plane-stress formulation.

The final results for the most refined mesh (2501 nodes and 192 fifth-order elements) are depicted in Figs. 5, 6, and 7, considering the three models (nH, MR, and BBC). The graph force–displacement obtained from the present formulation exhibits a more flexible behavior when compared to the reference solutions, in which the same geometry and material coefficients are adopted. The solutions obtained with the incompressible models (MR and BBC) in terms of the graph force–displacement are very close. This is expected, since the material coefficients for both models have been interpolated from the same experimental data. The stress concentration and the strong mesh distortion reported in Düster et al. (2003) can be seen in Fig. 7. Although the stress field around the upper left corner is probably three-dimensional, the singularity point and the overall behavior of the panel can be reproduced by the present plane-stress formulation for sufficiently refined meshes.

Partially loaded membrane

As the second example, the partially loaded plane rubber block depicted in Fig. 8 is considered. This problem has been presented by Reese et al. (1999) to assess the performance of a new stabilized mixed finite-element formulation developed to avoid hourglass instabilities. According to Reese (2003), this example is frequently employed to test element formulations in a problem involving extreme mesh distortions combined with high compression levels. Due to the symmetry regarding the plane $x_1 = 0.0$, only one half of the membrane is discretized. The horizontal displacement (u_1) of the upper edge and the vertical displacement (u_2) of the lower face are constrained. The uniform pressure load is divided into 100 steps. In this example, only the nH model is employed and the material coefficients are the same as those adopted for the Cook's membrane (see Fig. 2).

The convergence analysis is performed in terms of the final vertical displacement of points A and B, as well as the final equivalent stress at points C and D (see Fig. 8). As expected, the results converge with mesh refinement, according to Table 3. However, this convergence does not

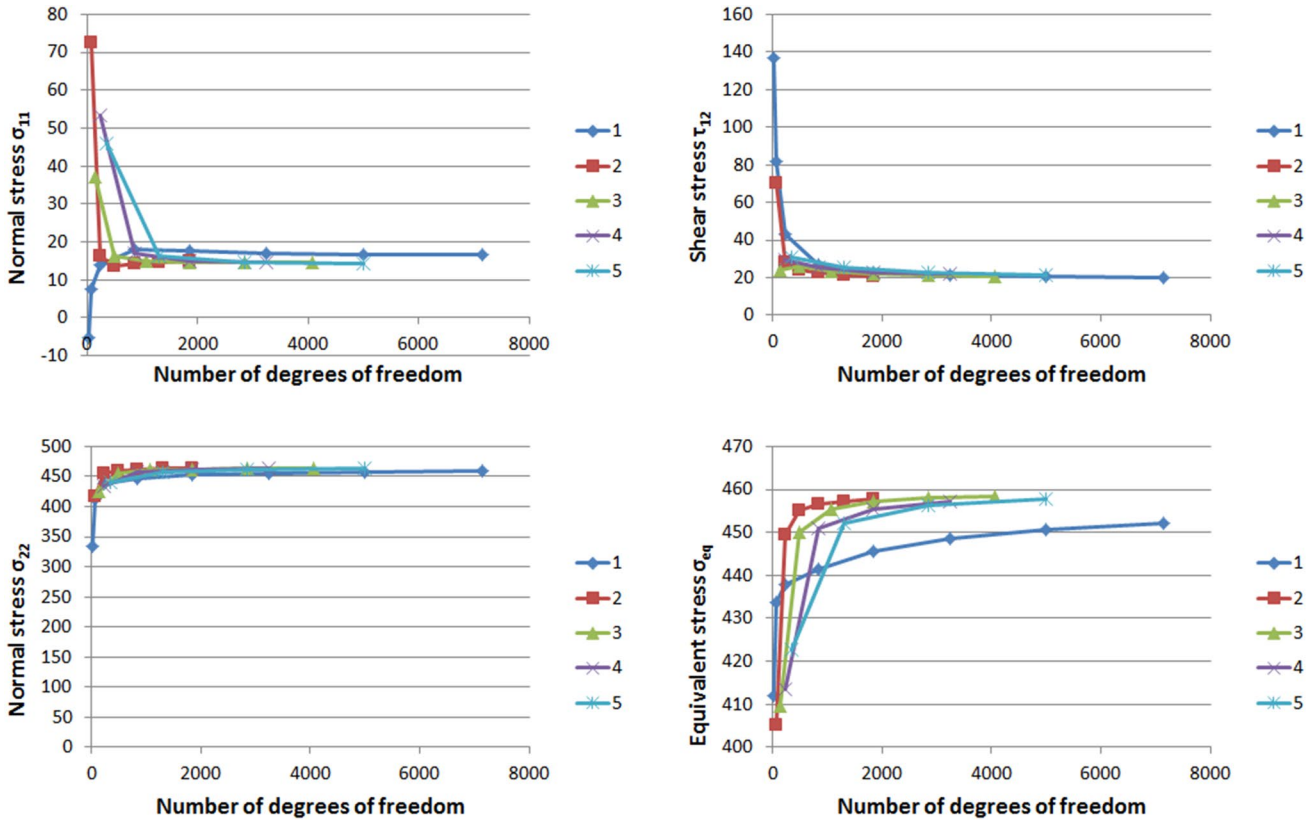

Fig. 4 Convergence analysis in terms of stresses (in kPa) for the BBC model at point A (44.0, 58.6667)

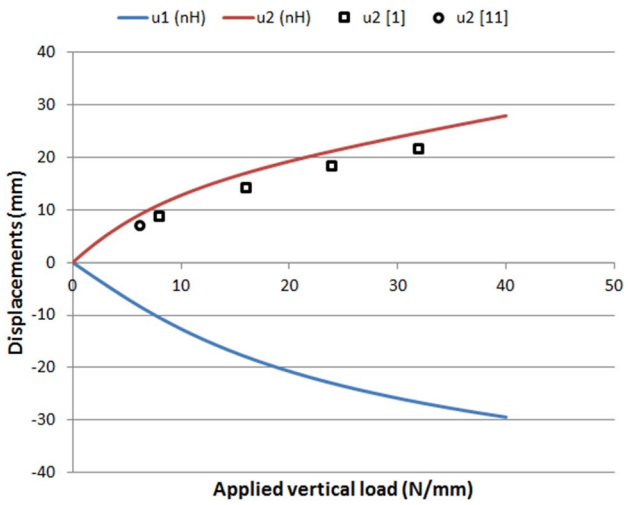

Fig. 5 Graphs force–displacement for the nH model

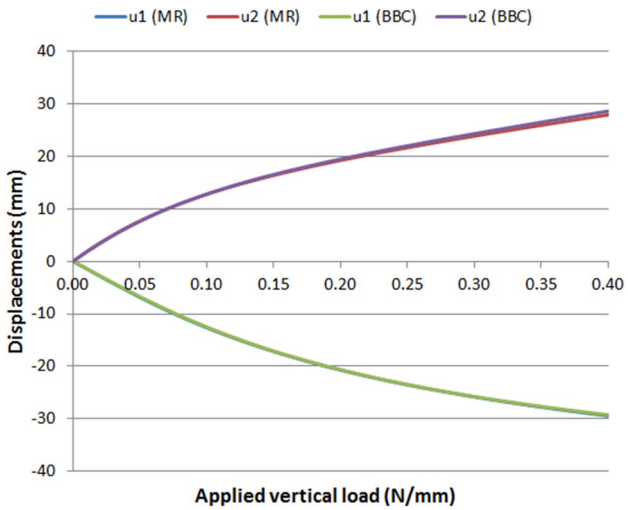

Fig. 6 Graphs force–displacement for the incompressible models

follow the usual behavior, in which the structure flexibility and, thus, the displacements increase when the mesh refinement becomes higher. For example, the value of the vertical displacement of point B decreases by refining the mesh, except for the linear order. Moreover, the approximations that provide the highest displacements in Table 3 are the meshes with 18 and 72 quadratic elements, and not the most refined one (162 fourth-order elements). Another example is the oscillatory behavior of displacements for the linear and quadratic elements: when the mesh is refined, the displacement of points A and B may become higher or smaller depending on the number of elements. Nevertheless,

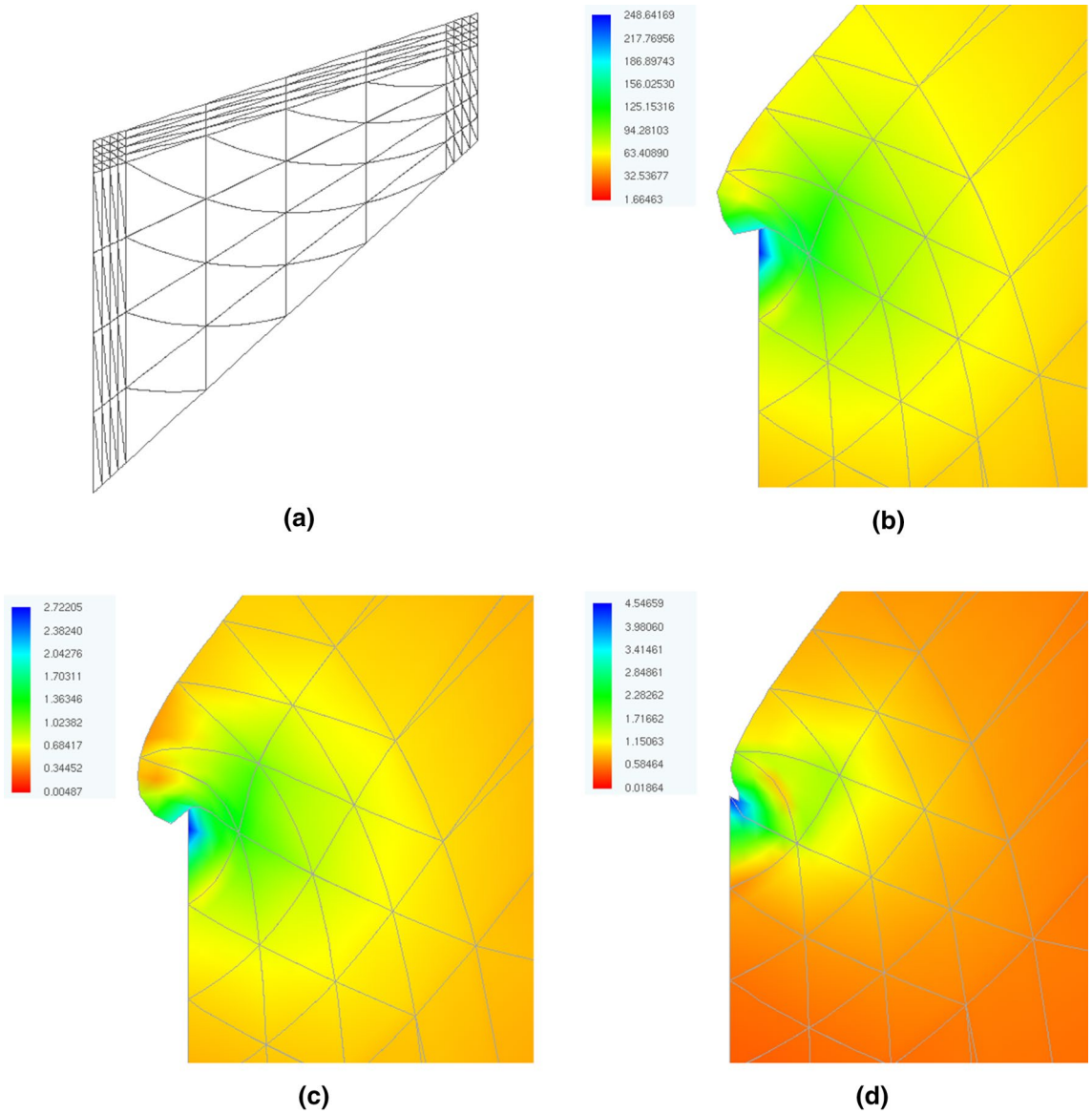

Fig. 7 Final distribution of the equivalent Cauchy stress around the left upper corner for the most refined mesh: **a** initial mesh; **b** nH model; **c** MR model; **d** BBC model

the values of displacements are not changed significantly with mesh refinement. In other words, the displacement field of the present example can be obtained even with coarse meshes. This convergence behavior in terms of nodal displacements has also been reported in Angoshtari et al. (2017) for point A. The final value for the vertical displacement of point A obtained in such reference is −6.5, which is smaller than the present result. Although the final pressure applied and the material coefficients are the same, this discrepancy is certainly due to the fact the hyperelastic neo-Hookean model adopted in that work is the 2D version for plane strain conditions.

Considering the equivalent stress levels at points C and D, the rate of convergence is improved by increasing the element order. Except for the two less refined linear and quadratic meshes (18 and 72 elements), the equivalent stresses always converge when the number of elements is increased. In summary, the most appropriate orders for the present example, in the context of Table 3, are probably the cubic and fourth degrees, because of the stability of values regarding displacements and stresses. As in the first example, the processing times and number of iterations required are small, even for the most refined discretizations.

The final distributions of the equivalent stress are provided in Fig. 9 considering the four meshes with 162

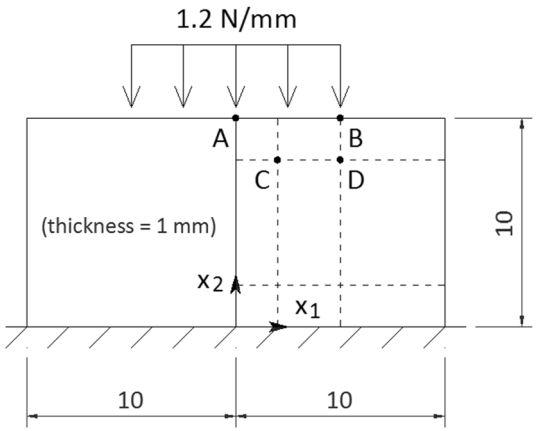

Fig. 8 Partially loaded membrane: geometry, boundary conditions, and base mesh

elements. As in the work of Angoshtari et al. (2017), the equivalent stresses are higher at the lower region close to the symmetry plane for all the meshes. However, for the cubic and fourth degrees, the highest values are found near point B. The high level of compression (approximately 87% at point A) and the strong mesh distortion depicted in Fig. 9 can be reproduced precisely by the present formulation.

Rubber sealing

The third and last example is the compression of the rubber sealing depicted in Fig. 10. This is a more realistic problem, because similar rubber seals are employed in cars, for example. The geometry of the problem has been extracted from Angoshtari et al. (2017), in which the material behavior for this problem is described by a compressible hyperelastic Ogden model. The numerical simulation is performed via a displacement control applied uniformly to the upper face in 100 steps ($\Delta u_2 = -0.022$ mm). Only one half of the sealing is used since the problem is symmetric. The upper face is restricted in x_1-direction and the lower face is constrained in both directions. Due to the complexity of the displacement and stress fields near the corners of the sealing, numerical instabilities may arise along the simulation, depending on the finite element adopted.

The convergence analysis in this case is performed in terms of the applied vertical force and the equivalent stress at some specific points. Again, results converge with mesh refinement (see Table 4). As expected, the linear order elements present a poor rate of convergence regarding applied forces and stresses. The high orders provide a convergence behavior similar to the most efficient mixed formulation employed in Angoshtari et al. (2017). Some final distributions are provided in Fig. 11 considering the most refined

Table 3 Convergence analysis for displacements and equivalent stresses

ORD	NDOF	NE	PT (s)	TNI	u_2 (A)	u_2 (B)	σ_{eq} (C)	σ_{eq} (D)
1	32	18	1	300	−8.45	−6.51	284.59	124.25
	98	72	1	300	−8.77	−6.55	255.39	99.85
	100	162	1	200	−8.86	−6.55	254.53	88.46
	338	288	1	260	−8.89	−6.56	258.60	82.48
	1250	1152	2	214	−8.86	−6.59	273.17	75.65
	2738	2592	4	207	−8.81	−6.61	283.27	76.41
	4802	4608	8	200	−8.76	−6.62	290.58	77.60
	7442	7200	13	200	−8.73	−6.62	296.02	78.40
2	98	18	1	300	−8.91	−6.77	272.72	116.04
	338	72	1	300	−8.68	−6.78	300.23	58.83
	722	162	3	300	−8.67	−6.76	304.76	64.61
	1250	288	3	219	−8.67	−6.74	311.30	70.87
	1922	450	6	213	−8.67	−6.73	314.77	74.61
3	200	18	2	300	−8.66	−6.76	311.55	57.91
	722	72	3	300	−8.67	−6.74	324.35	73.45
	1568	162	4	219	−8.67	−6.71	322.23	77.67
	2738	288	6	209	−8.67	−6.70	322.07	78.57
4	338	18	5	300	−8.66	−6.72	317.27	40.11
	1250	72	7	258	−8.67	−6.69	328.85	78.95
	2738	162	12	209	−8.67	−6.67	328.49	79.10

ORD, element order; NDOF, number of degrees of freedom; NE, number of elements; PT (s), processing time in second; TNI, total number of iterations; u_2 (X), vertical displacement of point X (mm); σ_{eq} (X), equivalent stress at point X (kPa)

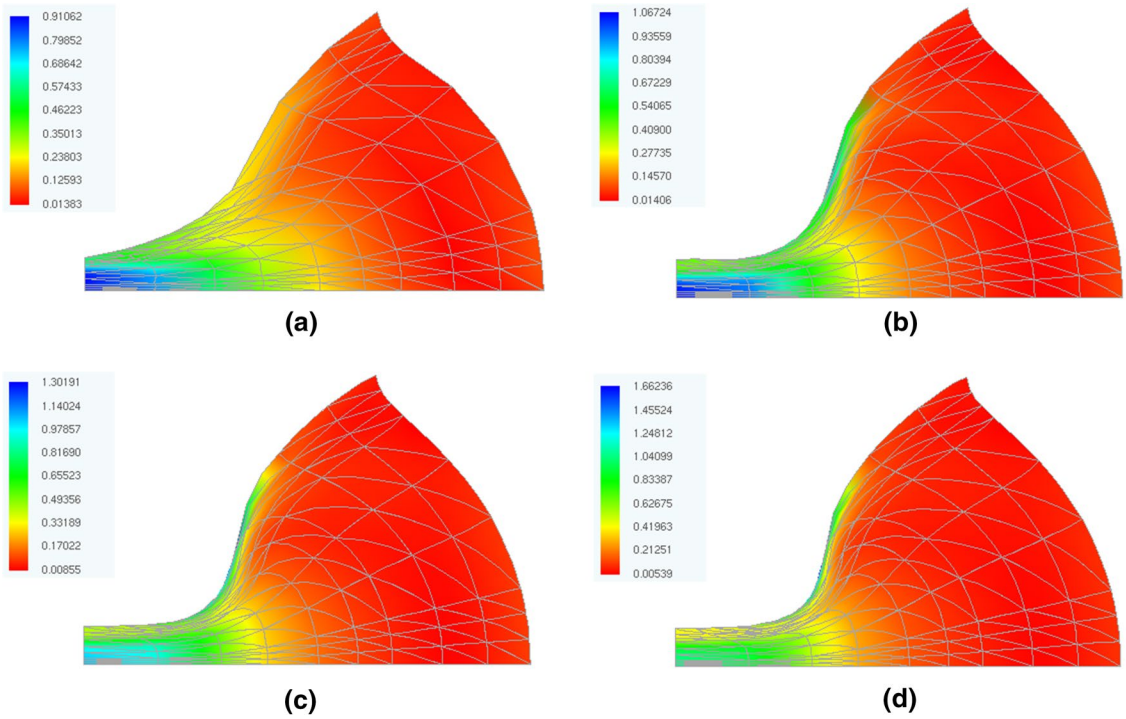

Fig. 9 Final distribution of the equivalent stress (in MPa) for meshes with 162 elements: **a** linear; **b** quadratic; **c** cubic; **d** fourth

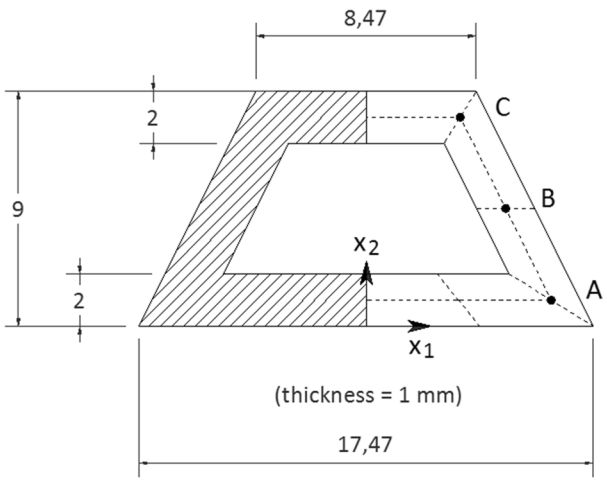

Fig. 10 Rubber sealing: geometry, boundary conditions, material data, and base mesh

mesh (2356 nodes and 180 fifth-order elements). One can see the large levels of deformations occurred in Fig. 11a, b, in terms of displacements, rotations, and mesh distortion. The distribution of the normal stretch component C_{33} in Fig. 11c gives an idea of the strain levels. Since the initial value of C_{33} is 1.0 and the highest final value is 1.791, it can be said that the maximum strain levels are moderate (neither infinitesimal nor extremely high). The equivalent stress field showed in Fig. 11d is similar to that obtained in Angoshtari et al. (2017), as the highest values occur at the same regions, indicating that both formulations provide comparable solutions. Moreover, if the maximum value for the equivalent Cauchy stress (88,248 kPa) is applied to a bar under uniaxial extension, the resultant longitudinal normal strain will be approximately 45%, considering the present material data and the analytical solution (see, for instance, the work of Pascon 2008). Such strain level can be considered moderately high for conventional engineering materials.

Table 4 Convergence analysis regarding applied forces and equivalent stresses

ORD	NDOF	NE	PT (s)	TNI	p_2	σ_{eq} (A)	σ_{eq} (B)	σ_{eq} (C)
1	36	20	1	400	− 312.49	363.76	398.85	273.26
	110	80	1	400	− 231.06	346.52	356.53	295.32
	378	320	1	500	− 184.22	341.75	318.72	250.30
	1394	1280	3	500	− 161.40	325.72	285.33	223.60
	3050	2880	8	544	− 153.41	312.68	268.52	216.86
	5346	5120	18	600	− 149.93	304.71	259.73	214.02
	8282	8000	35	655	− 147.12	299.90	255.21	212.63
2	110	20	1	400	− 195.09	360.35	380.08	291.69
	378	80	3	500	− 157.33	330.65	270.75	221.22
	806	180	5	500	− 148.48	310.04	248.03	212.46
	1394	320	8	500	− 145.00	298.48	245.40	212.15
	2142	500	14	558	− 142.91	292.79	246.84	212.66
	3050	729	21	600	− 142.23	289.98	248.04	213.05
	5346	1280	43	661	− 141.78	287.88	248.99	213.51
3	224	20	1	500	− 158.68	338.28	343.00	252.12
	806	80	3	500	− 144.46	303.53	244.44	204.27
	1748	180	11	600	− 141.82	289.25	243.49	206.56
	3050	320	20	638	− 141.23	286.45	246.65	209.14
	4712	500	37	740	− 141.26	285.71	247.69	210.60
4	378	20	6	500	− 148.24	308.08	343.76	243.04
	1394	80	14	600	− 141.55	297.17	244.37	200.44
	3050	180	42	700	− 141.09	288.39	243.94	204.44
5	572	20	23	530	− 142.71	289.88	332.96	245.53
	2142	80	40	500	− 141.28	298.70	244.69	200.73
	4712	180	117	645	− 140.66	288.23	243.77	204.30

ORD, element order; NDOF, number of degrees of freedom; NE, number of elements; PT (s), processing time in second; TNI, total number of iterations; p_2, final vertical reaction (N/mm); σ_{eq} (X), equivalent stress at point X (kPa)

Conclusions

A finite-element formulation to solve structural problems involving hyperelastic materials under plane-stress conditions has been developed. The elements are isoparametric triangular membranes of any order based on positional description. Lagrangian strain and stress measures from nonlinear solid mechanics are adopted: deformation gradient, right Cauchy–Green stretch tensor (and its invariants) and the second Piola–Kirchhoff stress tensor. Two hyperelastic models, usually employed for elastomers, have been selected: the compressible neo-Hookean model (nH); and the general incompressible Rivlin–Saunders model (RS). The 3D constitutive relations are condensed according to the plane-stress conditions and the resultant 2D compact forms for both models are provided. This condensation procedure requires the solution of nonlinear equations. It has been demonstrated that, in the case of the nH model, the expression to determine the out-of-plane normal strain is not explicit and, thus, a simple Newton algorithm is employed to obtain this strain component from the plane strains. The formulas to determine the consistent tangent operator, which is a fourth-order tensor required in the present Newton–Raphson method, are provided in the appendices considering the 2D constitutive forms.

Three structural problems involving hyperelastic materials under plane-stress conditions are analyzed to assess the performance of the present finite-element approach: the Cook's membrane, a bending-dominated problem with a singularity point; the partially loaded membrane, which presents a high level of compression together with severe mesh distortion; and the rubber sealing, a more realistic engineering problem. These benchmark problems have been employed to examine the convergence rate regarding displacements, applied forces, and stresses. Since the degree of approximation is generic, several meshes with different numbers of elements and orders (up to fifth degree) have been used to analyze each problem with the same computer code developed. As expected, mesh refinement provides more accurate results and the convergence rate obtained with the higher orders is similar to that presented by some mixed formulations from the scientific literature. The main advantage

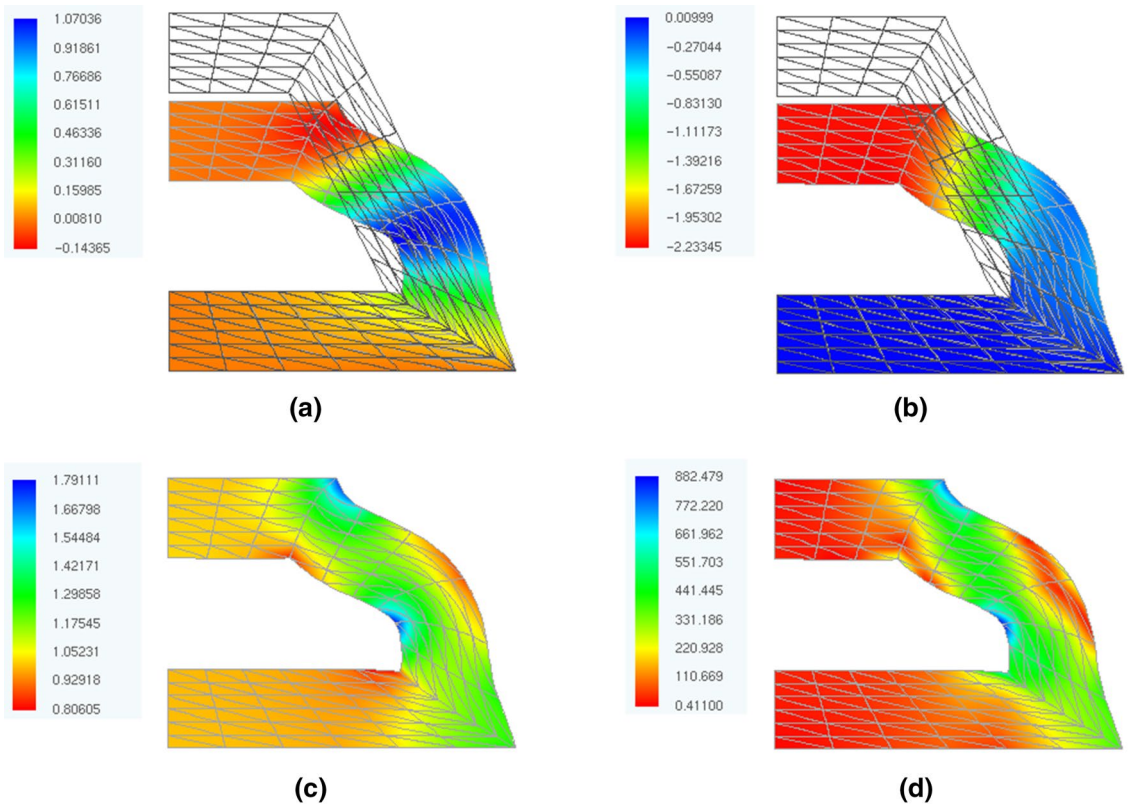

Fig. 11 Final results for the most refined mesh (2356 nodes and 180 fifth-order elements): **a** horizontal displacements (mm); **b** vertical displacements (mm); **c** stretch component C_{33}; **d** equivalent stress (kPa)

of the present method in comparison with these alternative formulations is the mathematical simplicity, i.e., no special techniques and no complex mathematical formulations are needed. Results also indicate that the finite-element formulation proposed here can predict the correct structural behavior in both incompressible and near-incompressible regimes. Therefore, in the context of the present paper, general locking problems are avoided by mesh refinement. These locking phenomena are usually associated with the incompressibility assumption, stress concentration, mesh distortion, complex geometries, and bending-dominated problems. It should also be highlighted that the so-called hourglass instabilities, which are common in mixed formulations, have not been observed in the present analyses. In short, the finite-element formulation proposed here is showed to be simple, robust, accurate, and reliable. Thus, it can be extended to other types of numerical analyses with highly deformable materials under plane-stress conditions as, for example, elastoplasticity, viscoelasticity, thermoelasticity and anisotropy.

Some contributions of the present study can be cited: convergence regarding displacements and stresses; use of higher orders; and development of the consistent tangent operator for the hyperelastic models nH and RS in plane-stress conditions. Although it is well known that mesh refinement leads to more accurate results, the influence of the mesh on the stress field and the use of higher orders of approximation are rarely seen. Moreover, some details of the consistent tangent operator provided here are usually omitted.

Acknowledgements The author thanks all the support provided by the Materials Engineering Department (Lorena School of Engineering, University of São Paulo), as well as the Structural Engineering Department (São Carlos School of Engineering, University of São Paulo) for granting remote access to their cluster.

Funding This research did not receive any specific grant from funding agencies in the public, commercial, or not-for-profit sectors.

Appendix 1: Consistent tangent operator for neo-Hookean model

The derivatives of the transverse strain C_{33} and the inverse matrix $\mathbf{C}^{-1}$ in terms of tensor $\mathbf{C}$, considering the neo-Hookean model (39), are provided in this section. First, one can define the following auxiliary scalar variable from (17):

$$f = C_{11}C_{22} - C_{12}^2 = \frac{\left\{\exp\left[\frac{\mu}{K}\left(1 - C_{33}\right)\right]\right\}^2}{C_{33}}. \tag{46}$$

As mentioned before, the component C_{33} cannot be explicitly obtained from the plane strain components. However, the scalar variable f can be determined from C_{33}. Therefore, the expression to obtain the derivative of C_{33} is as follows:

$$\frac{\partial C_{33}}{\partial \mathbf{C}} = \frac{\partial C_{33}}{\partial f}\frac{\partial f}{\partial \mathbf{C}} = \left(\frac{\partial f}{\partial C_{33}}\right)^{-1}\frac{\partial f}{\partial \mathbf{C}} \tag{47}$$

$$\frac{\partial f}{\partial C_{33}} = -\frac{\left\{\exp\left[\frac{\mu}{K}\left(1 - C_{33}\right)\right]\right\}^2}{C_{33}^2} - 2\frac{\mu}{K}\frac{\left\{\exp\left[\frac{\mu}{K}\left(1 - C_{33}\right)\right]\right\}^2}{C_{33}} \tag{48}$$

$$\frac{\partial f}{\partial \mathbf{C}} = \begin{bmatrix} C_{22} & -2C_{12} \\ -2C_{12} & C_{11} \end{bmatrix}. \tag{49}$$

The other derivative that appears in (38) is obtained from the definition of the inverse matrix $\mathbf{C}^{-1}$ considering only the plane components:

$$\mathbf{C}^{-1} = \frac{1}{C_{11}C_{22} - C_{12}^2}\begin{bmatrix} C_{22} & -C_{12} \\ -C_{12} & C_{11} \end{bmatrix} = \frac{1}{f}\mathrm{adj}(\mathbf{C}) \tag{50}$$

$$\frac{\partial \mathbf{C}^{-1}}{\partial \mathbf{C}} = \mathrm{adj}(\mathbf{C}) \otimes \frac{\partial}{\partial \mathbf{C}}\left(\frac{1}{f}\right) + \frac{1}{f}\frac{\partial \mathrm{adj}(\mathbf{C})}{\partial \mathbf{C}} \tag{51}$$

$$\frac{\partial}{\partial \mathbf{C}}\left(\frac{1}{f}\right) = -\frac{1}{f^2}\frac{\partial f}{\partial \mathbf{C}} \tag{52}$$

$$\frac{\partial(\mathrm{adj}C)_{11}}{\partial C_{22}} = \frac{\partial(\mathrm{adj}C)_{22}}{\partial C_{11}} = -\frac{\partial(\mathrm{adj}C)_{12}}{\partial C_{12}} = -\frac{\partial(\mathrm{adj}C)_{21}}{\partial C_{12}} = 1, \tag{53}$$

where $\mathrm{adj}(\mathbf{C})$ denotes the adjugate matrix of $\boldsymbol{C}$. The remaining components of the fourth-order tensor $\partial \mathrm{adj}(\mathbf{C})/\partial \mathbf{C}$ are null.

Appendix 2: Consistent tangent operator for Rivlin–Saunders model

The derivatives in terms of tensor $\boldsymbol{C}$ that appear in the Rivlin–Saunders model (43) are given in this "Appendices 1 and 2". First, the normal out-of-plane component of the isochoric stress tensor is differentiated in respect to $\boldsymbol{C}$:

$$\left(S_{\mathrm{iso}}\right)_{33} = \alpha + \beta\left(tr\mathbf{C} + C_{33}\right) \tag{54}$$

$$\frac{\partial\left(S_{\mathrm{iso}}\right)_{33}}{\partial \mathbf{C}} = \frac{\partial \alpha}{\partial \mathbf{C}} + \frac{\partial \beta}{\partial \mathbf{C}}\left(tr\mathbf{C} + C_{33}\right) + \beta\left(\frac{\partial tr\mathbf{C}}{\partial \mathbf{C}} + \frac{\partial C_{33}}{\partial \mathbf{C}}\right) \tag{55}$$

$$\frac{\partial \alpha}{\partial \mathbf{C}} = 2\frac{\partial^2 \psi_{\mathrm{iso}}}{\partial i_1^{\mathrm{iso}}\partial i_1^{\mathrm{iso}}}\frac{\partial i_1^{\mathrm{iso}}}{\partial \mathbf{C}} = 2\sum_{i,j} i(i-1)c_{ij}\left(i_1^{\mathrm{iso}} - 3\right)^{i-2}\left(i_2^{\mathrm{iso}} - 3\right)^{j}\frac{\partial tr\mathbf{C}}{\partial \mathbf{C}} \tag{56}$$

$$\frac{\partial \beta}{\partial \mathbf{C}} = 2\frac{\partial^2 \psi_{\mathrm{iso}}}{\partial i_2^{\mathrm{iso}}\partial i_2^{\mathrm{iso}}}\frac{\partial i_2^{\mathrm{iso}}}{\partial \mathbf{C}} = 2\sum_{i,j} j(j-1)c_{ij}\left(i_1^{\mathrm{iso}} - 3\right)^{i}\left(i_2^{\mathrm{iso}} - 3\right)^{j-2}\frac{\partial i_2^{\mathrm{iso}}}{\partial \mathbf{C}}. \tag{57}$$

The derivative of C_{33} is performed considering the incompressibility condition:

$$\begin{aligned}\frac{\partial C_{33}}{\partial \mathbf{C}} &= \frac{\partial}{\partial \mathbf{C}}\left(\frac{1}{C_{11}C_{22} - C_{12}^2}\right) \\ &= -\frac{1}{\left(C_{11}C_{22} - C_{12}^2\right)^2}\begin{bmatrix} C_{22} & -C_{12} \\ -C_{12} & C_{11} \end{bmatrix} \\ &= -\frac{1}{f^2}\mathrm{adj}(\mathbf{C}),\end{aligned} \tag{58}$$

where f is another scalar auxiliary variable. Since the first invariant $i_1^{\mathrm{iso}} = tr\mathbf{C}$ depends on C_{33}, which, in turn, depends on the plane strains, the derivative $\partial tr\mathbf{C}/\partial \mathbf{C}$ results in the following:

$$\frac{\partial tr\mathbf{C}}{\partial \mathbf{C}} = \left(\frac{\partial tr\mathbf{C}}{\partial \mathbf{C}}\right)_{3D} + \frac{\partial tr\mathbf{C}}{\partial C_{33}}\frac{\partial C_{33}}{\partial \mathbf{C}} = \mathbf{I} + \frac{\partial tr\mathbf{C}}{\partial C_{33}}\frac{\partial C_{33}}{\partial \mathbf{C}} = \mathbf{I} + \frac{\partial C_{33}}{\partial \mathbf{C}}, \tag{59}$$

where $(\partial tr\mathbf{C}/\partial \mathbf{C})_{3D}$ is the three-dimensional derivative of i_1^{iso}, determined for the case in which the component C_{33} is independent of the plane strains. A similar procedure can be employed to define the derivative of the second invariant:

$$\begin{aligned}\frac{\partial i_2^{\mathrm{iso}}}{\partial \mathbf{C}} &= \left(\frac{\partial i_2^{\mathrm{iso}}}{\partial \mathbf{C}}\right)_{3D} + \frac{\partial i_2^{\mathrm{iso}}}{\partial C_{33}}\frac{\partial C_{33}}{\partial \mathbf{C}} = \frac{\partial i_2^{\mathrm{iso}}}{\partial \mathbf{C}} \\ &+ \frac{\partial i_2^{\mathrm{iso}}}{\partial C_{33}}\frac{\partial C_{33}}{\partial \mathbf{C}} = (tr\mathbf{C})\mathbf{I} + \mathbf{C} + \left(tr\mathbf{C} + C_{33}\right)\frac{\partial C_{33}}{\partial \mathbf{C}},\end{aligned} \tag{60}$$

where $\left(\partial i_2^{\text{iso}}/\partial \mathbf{C}\right)_{3D}$ is the three-dimensional derivative of i_2^{iso}, determined for an independent component C_{33}. The reason for emphasizing the abovementioned 3D derivatives is to distinguish them from the 2×2 matrices $\partial tr\mathbf{C}/\partial\mathbf{C}$ and $\partial i_2^{\text{iso}}/\partial\mathbf{C}$, which are compact forms determined for the plane-stress conditions.

The third derivative in (43) is related to the volumetric stress tensor:

$$\frac{\partial \mathbf{s}_{\text{vol}}}{\partial \mathbf{C}} = \frac{\partial}{\partial \mathbf{C}}\left(J\mathbf{C}^{-1}\right) = \frac{\partial \mathbf{C}^{-1}}{\partial \mathbf{C}}. \tag{61}$$

The last derivative in the above expression is given in (51).

Finally, differentiating the isochoric stress tensor $\boldsymbol{S}_{\text{iso}}$ with respect to $\boldsymbol{C}$ leads to the following:

$$\begin{aligned}\frac{\partial \mathbf{S}_{\text{iso}}}{\partial \mathbf{C}} &= \frac{\partial}{\partial \mathbf{C}}\left(\alpha\frac{\partial i_1^{\text{iso}}}{\partial \mathbf{C}} + \beta\frac{\partial i_2^{\text{iso}}}{\partial \mathbf{C}}\right) = \frac{\partial i_1^{\text{iso}}}{\partial \mathbf{C}} \otimes \frac{\partial \alpha}{\partial \mathbf{C}} \\ &+ \alpha\frac{\partial^2 i_1^{\text{iso}}}{\partial \mathbf{C}\partial \mathbf{C}} + \frac{\partial i_2^{\text{iso}}}{\partial \mathbf{C}} \otimes \frac{\partial \beta}{\partial \mathbf{C}} + \beta\frac{\partial^2 i_2^{\text{iso}}}{\partial \mathbf{C}\partial \mathbf{C}}\end{aligned} \tag{62}$$

$$\begin{aligned}\frac{\partial \alpha}{\partial \mathbf{C}} &= 2\left[\sum_{i,j} i(i-1)c_{ij}\left(i_1^{\text{iso}}-3\right)^{i-2}\left(i_2^{\text{iso}}-3\right)^{j}\right]\frac{\partial i_1^{\text{iso}}}{\partial \mathbf{C}} \\ &+ 2\left[\sum_{i,j} ijc_{ij}\left(i_1^{\text{iso}}-3\right)^{i-1}\left(i_2^{\text{iso}}-3\right)^{j-1}\right]\frac{\partial i_2^{\text{iso}}}{\partial \mathbf{C}}\end{aligned} \tag{63}$$

$$\begin{aligned}\frac{\partial \beta}{\partial \mathbf{C}} &= 2\left[\sum_{i,j} ijc_{ij}\left(i_1^{\text{iso}}-3\right)^{i-1}\left(i_2^{\text{iso}}-3\right)^{j-1}\right]\frac{\partial i_1^{\text{iso}}}{\partial \mathbf{C}} \\ &+ 2\left[\sum_{i,j} j(j-1)c_{ij}\left(i_1^{\text{iso}}-3\right)^{i}\left(i_2^{\text{iso}}-3\right)^{j-2}\right]\frac{\partial i_2^{\text{iso}}}{\partial \mathbf{C}}\end{aligned} \tag{64}$$

$$\frac{\partial^2 i_1^{\text{iso}}}{\partial \mathbf{C}\partial \mathbf{C}} = \frac{\partial}{\partial \mathbf{C}}\left(\mathbf{I} + \frac{\partial C_{33}}{\partial \mathbf{C}}\right) = \frac{\partial^2 C_{33}}{\partial \mathbf{C}\partial \mathbf{C}} \tag{65}$$

$$\begin{aligned}\frac{\partial^2 i_2^{\text{iso}}}{\partial \mathbf{C}\partial \mathbf{C}} &= \frac{\partial}{\partial \mathbf{C}}\left[(tr\mathbf{C})\mathbf{I} + \mathbf{C} + \left(tr\mathbf{C} + C_{33}\right)\frac{\partial C_{33}}{\partial \mathbf{C}}\right] \\ &= \mathbf{I}\otimes\mathbf{I} + \mathbf{II} + \frac{\partial C_{33}}{\partial \mathbf{C}} \otimes \left(\frac{\partial i_1^{\text{iso}}}{\partial \mathbf{C}} + \frac{\partial C_{33}}{\partial \mathbf{C}}\right) \\ &+ \left(tr\mathbf{C} + C_{33}\right)\frac{\partial^2 C_{33}}{\partial \mathbf{C}\partial \mathbf{C}}\end{aligned} \tag{66}$$

$$\frac{\partial^2 C_{33}}{\partial \mathbf{C}\partial \mathbf{C}} = \frac{\partial}{\partial \mathbf{C}}\left[-\frac{1}{f^2}\text{adj}(\mathbf{C})\right] = \frac{2}{f^3}\text{adj}(\mathbf{C}) \otimes \frac{\partial f}{\partial \mathbf{C}} - \frac{1}{f^2}\frac{\partial \text{adj}(\mathbf{C})}{\partial \mathbf{C}}, \tag{67}$$

where $\mathbf{O}$ is the fourth-order zero tensor; and $\mathbf{II}$ denotes the fourth-order identity tensor ($\mathbf{II} : \mathbf{A} = \mathbf{A}$ for every second-order tensor $\boldsymbol{A}$). The derivatives $\partial f/\partial\mathbf{C}$ and $\partial\text{adj}(\mathbf{C})f/\partial\mathbf{C}$ are provided in expressions (49) and (53), respectively.

References

Angoshtari A, Shojaei MF, Yavari A (2017) Compatible-strain mixed finite element methods for 2D compressible nonlinear elasticity. Comput Methods Appl Mech Eng 313:596–631

Bechir H, Boufala K, Chevalier Y (2002) Strain energy density function for carbon black filled rubber vulcanized for industrial applications. Mech Ind 3:245–252

Chavan KS, Lamichhane BP, Wohlmuth BI (2007) Locking-free finite element methods for linear and nonlinear elasticity in 2D and 3D. Comput Methods Appl Mech Eng 196:4075–4086

Cook RD, Malkus DS (1989) Concepts and applications of finite element analysis, 3rd edn. Wiley, New York

Crisfield MA (2000) Non-linear finite element analysis solids and structure. Wiley, Chichester

Düster A, Hartmann S, Neff E (2003) p-FEM applied to finite isotropic hyperelastic bodies. Comput Methods Appl Mech Eng 192(2003):5147–5166

Holzapfel GA (2000) Nonlinear solid mechanics: a continuum approach for engineering. Wiley, Chichester

Jabareen M, Rubin MB (2014) A six node plane strain triangular Cosserat Point Element (CPE) for nonlinear elasticity. Int J Eng Sci 74:118–142

Kirchner E, Reese S, Wriggers P (1997) A finite element method for plane stress problems with large elastic and plastic deformations. Commun Numer Methods Eng 13:963–976

Mooney R (1940) A theory of large elastic deformation. J Appl Phys 11:582–592

Mostafa M, Sivaselvan MV, Felippa CA (2013) Reusing linear finite elements in material and geometrically nonlinear analysis: application to plane stress problems. Finite Elem Anal Des 69:62–72

Pascon JP (2008) Constitutive models for hyperelastic materials: study and numerical implementation. Master's Dissertation (in Portuguese), Structural Engineering Department, São Carlos School of Engineering, University of São Paulo

Pascon JP (2012) On nonlinear constitutive models for functionally graded materials exhibiting large strains: numerical implementation in geometrically nonlinear formulation. Ph.D. Thesis (in Portuguese), Structural Engineering Department, São Carlos School of Engineering, University of São Paulo

Pascon JP, Coda HB (2012) Analysis of elastic functionally graded materials under large displacements via high-order tetrahedral elements. Finite Elem Anal Des 50:33–47

Pascon JP, Coda HB (2013) Large deformation analysis of homogeneous rubber-like materials via shell finite elements. Latin Am J Solids Struct 10:1177–1209

Pascon JP, Coda HB (2015) Large deformation analysis of functionally graded elastoplastic materials via solid tetrahedral finite elements. Comput Struct 146:59–75

Pascon JP, Coda HB (2017) Finite deformation analysis of visco-hyperelastic materials via solid tetrahedral finite elements. Finite Elem Anal Des 133:25–41

Reese S (2003) On a consistent hourglass stabilization technique to treat large inelastic deformations and thermo-mechanical coupling in plane strain problems. Int J Numer Methods Eng 57:1095–1127

Reese S, Küssner M, Reddy BD (1999) A new stabilization technique for finite elements in non-linear elasticity. Int J Numer Methods Eng 44:1617–1652

Rivlin RS (1956) Rheology theory and applications, vol 1. Academic Press, New York

Simo JC, Rifai MS (1990) A class of mixed assumed strain methods and the method of incompatible modes. Int J Numer Methods Eng 29:1595–1638

Sze KY, Zheng SJ, Lo SH (2004) A stabilized eighteen-node solid element for hyperelastic analysis of shells. Finite Elem Anal Des 40:319–340

Yeoh OH (1990) Characterization of elastic properties of carbon-black-filled rubber vulcanizates. Rubber Chem Technol 63:792–805

Yeoh OH (1997) Hyperelastic material models for finite element analysis of rubber. J Nat Rubber Res 12:142–153